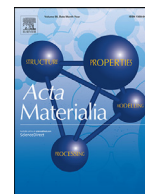# Complexions and grain growth retardation: First-principles modeling of phase boundaries in WC-Co cemented carbides at elevated temperatures

(article starts on next page)

Full length article

Complexions and grain growth retardation: First-principles modeling of phase boundaries in WC-Co cemented carbides at elevated temperatures

Erik Fransson*, Martin Gren, Göran Wahnström

Chalmers University of Technology, Department of Physics, SE-412 96 Gothenburg, Sweden

ABSTRACT

WC-Co cemented carbides combine superb hardness with high toughness making them ideal for usage in metal machining and in wear resistant tools. Controlling the WC grain size is important during sintering as grain size plays a crucial role for the mechanical properties of the material. Experimental studies have observed different growth rates and grain morphologies in W-rich and C-rich materials, but the mechanism behind this has not been clarified. Here, we consider the possibility of an interface-stabilized state, a complexion, at the WC/Co phase boundary in cemented carbides, namely thin WC films with cubic structure. An interfacial phase diagram is derived using ab-initio calculations and first-principles modeling. Cluster expansions are employed to model carbon vacancies and Monte Carlo simulations to sample the configurational entropy. Force-constant fitting is used to extract the harmonic free energy for ground-state structures and the effects from anharmonicity and electronic excitations are effectively incorporated from a companion study on WC bulk phases. We predict the stabilization of thin cubic WC films at liquid phase sintering temperatures but only at W-rich conditions. This is consistent with experimental findings where thin films with cubic stacking have been observed predominantly in W-rich materials. We use this knowledge to suggest an explanation for the observed different growth rates and grain morphologies in W-rich and C-rich cemented carbides.

1. Introduction

Liquid phase sintering (LPS) is an important process in materials science in which multiphase materials are produced by means of powder metallurgy. It involves sintering under conditions where solid grains coexist with a wetting liquid [1]. One such class of multiphase materials is cemented carbides, which consist of fine particles of a carbide cemented into a composite by a binder metal. The most common cemented carbide is produced by combining tungsten carbide (WC) with the binder metal cobalt (Co) [2–5]. Cemented carbides combine excellent hardness with high toughness and wear resistance. They are used in cutting and wear resistance tools and are of considerable technical and industrial importance [6,7].

The carbon content (the C/W ratio) must be controlled in a narrow concentration region when sintering WC-Co. This is to avoid formation of graphite (C/W too large) or a tungsten rich eta phase (C/W too small), which both are detrimental for the mechanical properties of the material [8]. Furthermore, when sintering WC-Co it is critical to control the grain growth of the carbide grains, as too large grains gives a softer and less wear resistant material [6,9]. It has been known for a long time that the growth rate of the carbide grains is larger under C-rich conditions (high carbon content) compared to W-rich conditions (low carbon content) [8,10–14]. However, the mechanism behind this behaviour is still not clarified [8,14].

Grain growth in cemented carbides proceeds mainly by dissolution/precipitation, i.e., smaller grains dissolves and larger grains grow to reduce the total interface energy in the material [8,10]. The limiting process for grain growth is either solute diffusion in the liquid binder phase or dissolution/precipitation. The latter is an interface reaction at the phase boundary between the liquid and a carbide grain. In cemented carbides the measured grain growth rate is slow compared with solute diffusion in the liquid phase and therefore the interface reaction is rate limiting [8,15]. Dissolution is

---

* Corresponding author.
  E-mail addresses: erikfr@chalmers.se (E. Fransson), martin.gren@chalmers.se (M. Gren), goran.wahnstrom@chalmers.se (G. Wahnström).

known to be rapid [16], and hence, precipitation is the rate limiting step [8,15,17].

The precipitation step is decomposed into two coupled processes. For faceted grains, as WC grains in cemented carbides, a new atomic layer first has to nucleate by atoms attaching to the carbide surface [18,19]. This is controlled by a nucleation energy barrier which can be reduced by defects at the surface [19,20]. Subsequently the nucleus grows laterally and a new atomic layer is created[15,21]. The interface reaction may therefore be controlled by either the nucleation process or the following lateral growth.

In a series of papers, Lay et al. investigated the microstructure evolution in WC-Co at liquid phase sintering conditions [22–24]. The effect of the C/W ratio was studied by using two different WC-Co compositions, one C-rich and one W-rich. The time evolution of the grain size and shape were investigated for an extended time, 10 hours, at 1450°C and the measured grown WC grains were found to be larger in the C-rich material compared with the W-rich material [23,24], consistent with previous studies [10–12]. Furthermore, they found that the WC grains were perfectly faceted in the C-rich material, whereas they observed steps on WC/Co phase boundaries in the W-rich material [22]. The occurrence of steps in W-rich WC-Co, in contrary to C-rich WC-Co, has also been observed by Kim et al. [25], Borgh et al. [26] and Roulon et al. [17]. However, why the grain morphology differs between C-rich and W-rich materials has not been understood.

Lay et al. also made an important observation, the presence of a different atomic stacking at the WC/Co phase boundaries [27]. The different stacking corresponded to an ultrathin film of cubic WC, not hexagonal WC, and it was only about two WC layers thick. The cubic stacking was observed very frequently in the W-rich material but more seldom in the C-rich material [27]. The same type of atomic stacking has also been observed by Liu et al. [28].

Tungsten carbide has a hexagonal crystal structure. Only at very high temperatures, above 2700°C, cubic WC becomes stable [29]. To obtain cubic stacking of WC at phase boundaries at considerably lower temperatures is therefore surprising. However, thin layers of cubic WC may be thermodynamically stabilized by interfacial effects at temperatures below 2700°C, similarly to thin film formation in doped cemented carbides [30]. If cubic WC films are present at phase boundaries, thermodynamically stabilized by interfacial effects, they may have a substantial impact on the growth behavior of the tungsten carbide grains.

In the present paper an atomic scale approach, based on density functional theory (DFT) calculations, is employed to derive a so called interfacial phase diagram [30] for thin cubic WC films at WC/Co phase boundaries. These interfacial structures are referred to as complexions[30–32]. We demonstrate that at LPS temperatures thin cubic WC films are, indeed, thermodynamically stabilized by interfacial effects in W-rich conditions but not in C-rich conditions. We use this knowledge to suggest an explanation for the different growth behavior in C-rich and W-rich cemented carbides, a long-standing issue within the hard metal research community.

2. Simplified model

Let us first introduce a simplified model to illustrate the idea behind the thin film formation. Consider a phase boundary between hexagonal WC and Co. Denote the interface energy as $\gamma_{\text{nofilm}} = \gamma_{\text{WC}^{\text{hex}}/\text{Co}}$. For a phase boundary with a thin film consisting of N layers of stoichiometric cubic WC, the interface energy can be approximated as

$$\gamma_{\text{film}} = \gamma_{\text{WC}^{\text{hex}}/\text{WC}^{\text{cub}}} + N(\Delta g + e) + \gamma_{\text{WC}^{\text{cub}}/\text{Co}} \tag{1}$$

where Δg is the difference in free energy between cubic and hexagonal bulk WC per layer of WC and e is the corresponding

elastic energy associated with the formation of the thin film. We then define the *relative interface energy* as

$$\Delta\gamma \equiv \gamma_{\text{film}} - \gamma_{\text{nofilm}} = \Gamma + N(\Delta g + e) \tag{2}$$

where

$$\Gamma = \gamma_{\text{WC}^{\text{hex}}/\text{WC}^{\text{cub}}} + \gamma_{\text{WC}^{\text{cub}}/\text{Co}} - \gamma_{\text{WC}^{\text{hex}}/\text{Co}}. \tag{3}$$

If $\Delta\gamma$ is negative, film formation is favourable. This simplified model was introduced in Ref. [33] and it gave a semi-quantitative description for $N \geq 2$.

Let us first consider the value for Γ. The interface energies between WC^{hex} and Co and between WC^{cub} and Co are quite different, $\gamma_{\text{WC}^{\text{hex}}/\text{Co}} = 1.13$ J/m² and $\gamma_{\text{WC}^{\text{cub}}/\text{Co}} = -1.30$ J/m², respectively (see Supplemental Material). We also need the cost to create the boundary between WC^{hex} and WC^{cub}. This is equal to $\gamma_{\text{WC}^{\text{hex}}/\text{WC}^{\text{cub}}} = 0.45$ J/m² (see Supplemental Material) and hence, we obtain $\Gamma = -2.0$ J/m². A negative value of Γ implies a tendency for film formation.

However, to create a thin film, layers of cubic WC have to be created. Cubic WC is thermodynamically unstable (at not too high temperatures) and this implies an energy cost, $(\Delta g + e)$, per cubic layer of WC. At $T = 0$K $\Delta g = 2.0$ J/m² and $e = 0.44$ J/m² for stoichiometric cubic WC (see Table 3). The relative interface energy becomes equal to $\Delta\gamma = 2.9$ J/m² for $N = 2$ and, the film does not form at zero Kelvin. With increasing temperature, though, Δg decreases and for stoichiometric WC Δg becomes zero at about 3000 K [29]. Therefore, since Γ is negative, this simplified model suggests that thin cubic films may form below 3000 K, maybe at liquid phase sintering temperatures.

Furthermore, the cubic phase can contain a large amount of carbon vacancies while the hexagonal phase is essentially stoichiometric [29]. The carbon chemical potential is lower if the material is in equilibrium with the eta phase (W-rich condition) compared with equilibrium with graphite (C-rich condition). This implies that film formation with non-stoichiometric cubic films is more favourable in W-rich conditions compared with C-rich conditions.

3. Structural models

The first step in determining the relative interface energy $\Delta\gamma$ in our atomic scale approach is to define suitable interfacial structures.

Experimental studies report thin WC films with cubic structure in undoped cemented carbides [27,28]. These thin films are frequently found in phase boundaries with a basal, i.e. (0001), WC interface plane [27]. The orientation of the WC^{cub} phase in thin cubic films has been reported as $\text{WC}^{\text{hex}}(0001)\|\text{WC}^{\text{cub}}(111)$ [27,28]. Furthermore, the most frequent orientation of the Co rich binder phase, which has a fcc structure, relative to WC^{hex} in WC-Co cemented carbides is reported to be $\text{WC}^{\text{hex}}(0001)\|\text{Co}^{\text{fcc}}(111)$ [27]. Based on this information the following orientation:

$$\text{WC}^{\text{hex}}(0001)\|\text{WC}^{\text{cub}}(111)\|\text{Co}(111)$$

is chosen for the model interfaces in this study.

In the WC hexagonal crystal structure layers of W and C are alternating and stacked in an $\ldots ABABAB \ldots$ sequence along the basal [0001] direction. Here, A corresponds a translation (in scaled coordinates) of the atomic layer by $(0, 0)$ and B by $(\frac{1}{3}, \frac{2}{3})$ in the interface plane. The cubic WC structure also has alternating layers of W and C along its [111] direction, however, the stacking sequence is $\ldots ABCABC \ldots$, where C corresponds to a translation of the atomic layer by $(\frac{2}{3}, \frac{1}{3})$. Hence, the WC^{hex} structure can be converted to a WC^{cub} structure by altering the stacking sequence.

The carbide phase can either be metal (M) or carbon (C) terminated towards Co. The interface energy is, at least, about 1 J/m²
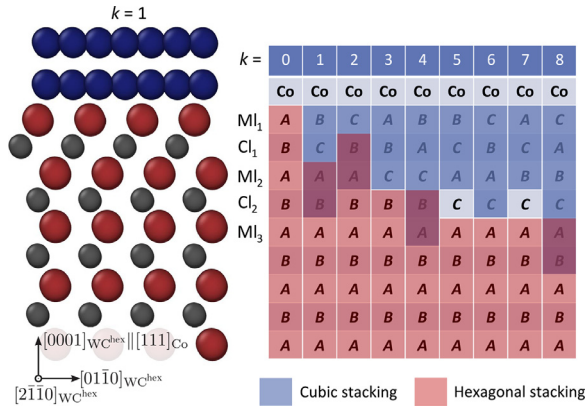
Fig. 1. Illustration of the nine different stackings. The left figure illustrates the atomic configuration at the WC/Co interface with the $k=1$ stacking generated by OVITO [35]. C, Co and W are represented by grey, blue and red atoms, respectively. The right table indicate the stacking sequences for the various ks and which atomic layers follows the hexagonal stacking (red) and the cubic stacking (blue). (For interpretation of the references to color in this figure legend, the reader is referred to the web version of this article.)

less if the carbide is terminated with a W plane compared with a C plane, for both hexagonal and cubic WC (see Supplemental Material) and, therefore, we restrict our study to metal (W) termination.

Allowing the first four layers (two W and two C) to deviate from the hexagonal stacking sequence eight unique thin film stacking sequences can be constructed [34]. These stacking sequences are illustrated in Fig. 1 together with the atomistic configuration for the $k=1$ stacking. The i:th metal layer counting from the cobalt is denoted Ml_i and the i:th carbon layer Cl_i. The $k=0$ stacking is simply the hexagonal WC(0001) in contact with Co(111).

There exists relations between the different stacking sequences. For example by extending the cubic phase by one WC layer for the $k=1$ stacking one obtains the $k=8$ stacking, similarly extending $k=2$ yields $k=4$.

In order to get small repeating unit cells with low strain in the Co phase the Co slab is oriented such that there is a 30° angle between WC^{hex} $[2\bar{1}\bar{1}0]$ and Co $[\bar{1}10]$[34]. This gives a unit cell with four Co atoms and three W or C atoms in each atomic layer along the interface normal direction [34].

In the Supplemental Material we present the calculated formation energy for single vacancies in the first four C layers of each stacking. Based on this, carbon vacancies will only be considered in the first two carbon layers in the thin film model systems, i.e., the C layers which may deviate from the hexagonal stacking. Further, no vacancies will be considered in the purely hexagonal stacking, $k=0$, since it is very unfavourable to introduce vacancies in the hexagonal structure [36]. The sites which can be occupied by either a carbon atom or a vacancy are denoted mixing sites and the number of mixing sites in the unit cell is $m=6$ (three per carbon layer). In the present work the carbon vacancy concentration x will be measured with respect to the number of mixing sites m.

4. Thermodynamics

4.1. Interface energy

The interface energy γ, i.e., the cost associated with creating an interface per interface area, is in general written as

$$\gamma(T) = \frac{1}{A}\left(G(T) - \sum_i N_i \mu_i(T)\right), \tag{4}$$

where A is the area of the interface, G the Gibbs free energy for the interface system at a given temperature T, and N_i and μ_i the

number of atoms of each species and their respective chemical potential [37]. The change in volume due to vacancies in the interface systems consider in this work gives rise to a $P\Delta V$ term much smaller than 0.1 meV per unit cell and can, therefore, safely be neglected.

For the interface systems it is convenient to consider the free energy per unit cell, g, which is related to the total free energy, G, via $G/A = g/a$, where a is the interface area per unit cell. The interface energy for a thin film structure with stacking k and carbon vacancy concentration x, at temperature T, can then be written as

$$\gamma_k(x, T) = \frac{1}{a}\left(g_k(x, T) - (1-x)m\mu_C(T) - \sum_{i\notin mix}\mu_i(T)\right), \tag{5}$$

where m is the number of mixing sites per unit cell and the last term is a sum over all atoms in the unit cell which are not part of the mixing sites.

In the real material the value of the carbon chemical potential μ_C may vary. We write

$$\mu_C(T) = \mu_{gra}(T) + \Delta\mu_C, \tag{6}$$

where $\mu_{gra}(T)$ denotes the free energy of graphite and $\Delta\mu_C$ denotes the shift away from graphite.

4.2. Free energy decomposition

We decompose the free energy of a film system, $g_k(x, T)$, into various terms as

$$g_k(x, T) = g_k(0, 0) - xm\mu_{gra}(0) + m\bar{g}_k^{mix}(x, T) + g_k^{har}(x, T) + g_k^{add}(x, T), \tag{7}$$

where $g_k(0, 0)$ is the energy of the interface system without vacancies and $\bar{g}_k^{mix}$ is defined as the mixing free energy per mixing site. Further, $g_k^{har}(x, T)$ is the harmonic vibrational free energy and the last term $g_k^{add}(x, T)$ is an additional term including anharmonic vibrational and electronic contributions.

We use the chemical potential of graphite at zero Kelvin as the slope for defining the mixing free energy. There is, consequently, no guarantee that $\bar{g}_k^{mix}(x=1, T) = 0$, which usually would be the case for mixing free energies. However, $\bar{g}_k^{mix}(x=0, T) = 0$, by construction. Further, the $g_k(0, 0)$ here does not include zero point effects, instead, this is included in $g_k^{har}(x, T)$. In the modeling of the purely hexagonal stacking $k=0$ no vacancies are included and, hence, its free energy can simply be decomposed as

$$g_0(0, T) = g_0(0, 0) + g_0^{har}(0, T) + g_0^{add}(0, T). \tag{8}$$

In the same manner the chemical potential of the graphite phase may be written as

$$\mu_{gra}(T) = \mu_{gra}(0) + \mu_{gra}^{vib}(T), \tag{9}$$

where $\mu_{gra}^{vib}(T)$ is the temperature dependent part of the chemical potential, which is predominantly due to harmonic vibrational contributions.

4.3. Relative interface energy

We can now define the *relative interface energy* as

$$\Delta\gamma_k(x, T) = \gamma_k(x, T) - \gamma_0(0, T), \tag{10}$$

where $\gamma_0(0, T)$ corresponds to the purely hexagonal stacking, i.e., the "nofilm" phase boundary.

The relative interface energy, $\Delta\gamma_k(x, T)$, can be split into five terms: zero Kelvin, configurational temperature effect, harmonic vibrational effect, additional anharmonic vibrational and electronic

contributions and environmental effects (due to change in carbon chemical potential) according to

$$\Delta\gamma_k = \Delta\gamma_k^0 + \Delta\gamma_k^{\mathrm{conf}} + \Delta\gamma_k^{\mathrm{har}} + \Delta\gamma_k^{\mathrm{add}} + \Delta\gamma_k^{\mathrm{env}}. \tag{11}$$

Here, the (x, T) have been dropped for simplicity. By using the equations above once can identify each of these four terms. The zero Kelvin part, $\Delta\gamma_k^0(x)$, can be written as

$$\Delta\gamma_k^0(x) = \frac{1}{a}\Big(g_k(0,0) - g_0(0,0) + m\bar{g}_k^{\mathrm{mix}}(x,0)\Big)$$
$$= \Delta\gamma_k^0(0) + \frac{1}{a}m\bar{g}_k^{\mathrm{mix}}(x,0), \tag{12}$$

the configurational temperature effect, $\Delta\gamma_k^{\mathrm{conf}}(x, T)$, as

$$\Delta\gamma_k^{\mathrm{conf}}(x,T) = \frac{1}{a}\Big(m\bar{g}_k^{\mathrm{mix}}(x,T) - m\bar{g}_k^{\mathrm{mix}}(x,0)\Big), \tag{13}$$

the vibrational effect, $\Delta\gamma_k^{\mathrm{har}}(x, T)$, as

$$\Delta\gamma_k^{\mathrm{har}}(x,T) = \frac{1}{a}\Big(g_k^{\mathrm{har}}(x,T) - g_k^{\mathrm{har}}(0,T) + mx\mu_{\mathrm{gra}}^{\mathrm{vib}}(T)\Big) \tag{14}$$

and the additional effect, $\Delta\gamma_k^{\mathrm{add}}(x, T)$, as

$$\Delta\gamma^{\mathrm{add}}(x,T) = \frac{1}{a}\Big(g_k^{\mathrm{add}}(x,T) - g_0^{\mathrm{add}}(0,T)\Big). \tag{15}$$

Finally, the environmental term, $\Delta\gamma_k^{\mathrm{env}}(x)$, becomes

$$\Delta\gamma_k^{\mathrm{env}}(x) = \frac{mx}{a}\Delta\mu_{\mathrm{C}} \tag{16}$$

and this term is thus the only part that depends on $\Delta\mu_{\mathrm{C}}$, which comes into play in Eq. (17).

4.4. Equilibrium stacking

The last step is to transform the relative interface energy from a function of (x, T) to a function of $(\Delta\mu_C, T)$

$$\Delta\gamma_k(\Delta\mu_C,T) = \min_x\{\Delta\gamma_k(x,T) : \Delta\mu_C\}, \tag{17}$$

where the minimization should be read as the minimum of $\Delta\gamma_k(x, T)$ with respect to x given $\Delta\mu_C$. The equilibrium stacking is obtained by whichever stacking k that minimizes $\Delta\gamma_k(\Delta\mu_C, T)$.

5. Computational methods

5.1. Alloy cluster expansions

In order to study the carbon vacancies in the films, we employ alloy cluster expansion (CE) [38,39]. The stacking sequences $k=1$, $k=2$, $k=4$ and $k=8$ were chosen for further analysis with CEs based on their vacancy formation energies (see Supplemental Material) and relative interface energies at 0 K $\Delta\gamma_k^0(0)$ (see Table 1) in combination with an anticipated decrease in Δg due to vibrational effects [36]. See Supplemental Material for more details on the selection of stacking sequences. Vacancies are considered only in the first two carbon layers (Cl$_1$ and Cl$_2$) (see Sect. 3). For $k=2$ the vacancy formation energy in the second carbon layer (Cl$_2$) was so high that this carbon layer was omitted from the CE for this stacking. However, in order to simplify the comparison with the other stackings, the carbon vacancy concentration for $k=2$ will still refer to two carbon layers throughout the paper.

The CE are constructed using the software ICET[40] and total energies from density functional theory (DFT) (see Appendix A), are used as reference energies. These models allow for very fast predictions of the mixing energy of different configurations and vacancy concentrations. We are, consequently, able to conduct ground-state searches via simulated annealing to obtain $\bar{g}_k^{\mathrm{mix}}(x, T = $

0). Further, it also makes it feasible to sample the temperature dependent part of the mixing free energy via Monte Carlo (MC) simulations.

For each stacking we use pair cutoff of 4.5 Å for constructing the CE, which yields about 15-20 parameters. Introducing triplets did not improve the cross-validation (CV) score, hence they (and higher order clusters) were not included in the expansions. For each stacking we used about 50-70 training structures. About half of these structures were randomly generated and the other half were low energy structures selected with guidance from an initial CE trained with the random structures. The CV root-mean-square error (RMSE) obtained for the finalized models were about 12 meV/site which corresponds to roughly 0.05 J/m^2.

5.2. Configurational free energy

In order to sample the configurational free energy of the CEs we use MC simulations using the standard Metropolis scheme[41]. We sample in the grand canonical ensemble for which (μ_C, T) are kept fixed. In this ensemble the trial move in the MC simulations consists of switching a carbon atom on the mixing sites to a vacancy or vise versa. All simulations are carried out for a supercell with 384 mixing sites using the MC functionality in ICET [40]. The probability P of observing a microstate with energy E and number of carbon atoms n_C is $P \propto \exp[-\beta(E - n_C\mu_C)]$[42]. In order to sample the configurational free energy we use the relation

$$\mu_{\mathrm{C}} = -\frac{1}{m}\frac{\partial g_k(x,T)}{\partial x}, \tag{18}$$

which in combination with Eq. (6), Eq. (7) and Eq. (9) (ignoring vibrational and additional contributions) yields

$$\Delta\mu_{\mathrm{C}} = -\frac{\partial\bar{g}_k^{\mathrm{mix}}(x,T)}{\partial x}. \tag{19}$$

Now, by integrating Eq. (19) we obtain the mixing free energy as

$$\bar{g}_k^{\mathrm{mix}}(x,T) = \bar{g}_k^{\mathrm{mix}}(0,T) - \int_0^x \Delta\mu_{\mathrm{C}}\mathrm{d}x, \tag{20}$$

where $\bar{g}_k^{\mathrm{mix}}(0, T)$ is known since, with $x = 0$, there is no configurational entropy. This means that $\bar{g}_k^{\mathrm{mix}}(x, T)$ can be calculated by running MC simulations with different values of $\Delta\mu_C$ which will produce different average concentrations $\langle x \rangle$ and, finally, carrying out the integration in Eq. (20).

This integration scheme can be carried out for multiple temperatures allowing for extraction of the mixing free energy surface in the (x, T)-plane. However, it will not work if a miscibility gap exists since this means that the vacancy concentration will not be a continuous function of $\Delta\mu_C$ [43]. For the relevant temperatures and concentrations in this work no miscibility gaps were observed in the MC simulations.

An example of the results from the MC simulations can be seen in Fig. 2 for stacking $k=4$. In a) the obtained vacancy concentration for a given $\Delta\mu_C$ is shown. As expected for a large $\Delta\mu_C$ the vacancy concentration is low as it becomes unfavorable to remove carbon atoms from the film and place them into the reference state. In b) the mixing energy and mixing free energy are shown for two temperatures, while the energetic part of $\bar{g}_k^{\mathrm{mix}}(x, T)$ increases with temperature the total mixing free energy decreases with temperature. In c) the mixing entropy is shown which indicates that, even at 2000 K, the system behaves quite differently from the ideal mixing behaviour. Specifically there exists an ordered state at $x = 0.167$ (without any vacancy-vacancy nearest neighbors) which is very strongly bounded giving rise to almost no configurational entropy even at 2000 K.

Table 1

Selected data for the thin films structures used in this paper. Number of cubic WC layers, N, are given for stackings: $k=1$, $k=2$, $k=4$ and $k=8$. In the thin-film orientation chosen in this study a WC layer will consist of one metal (W) layer and one C layer and the WC layer in overlapping regions, see Fig. 1, are regarded as half a cubic WC layer. The relative interface energy at 0 K without vacancies, $\Delta\gamma_k^0(0)$, is given for all stackings. The relative interface energy at 1750 K is given for $k=1$, $k=2$, $k=4$ and $k=8$ in equilibrium with either graphite ($\Delta\mu_C = 0$eV) or the eta (η_6) phase ($\Delta\mu_C = -0.163$eV). Here, x_{min} refers to vacancy concentration that minimizes the interface energy (cf. Eq. (17)). All interface energies are given in J/m^2.

k	1	2	3	4	5	6	7	8
N	1.5	1	-	2	-	-	-	2.5
$T = 0K,\ \Delta\mu_C = 0$								
$\Delta\gamma_k^0(0)$	1.65	0.54	1.57	2.75	1.72	2.41	3.0	4.05
$\Delta\gamma_k^0(x_{min})$	0.83	0.54	-	1.55	-	-	-	1.67
x_{min}	0.17	0.0	-	0.17	-	-	-	0.5
$T = 1750K,\ \Delta\mu_C = 0$								
$\Delta\gamma_k(x_{min})$	0.27	0.19	-	0.54	-	-	-	0.63
x_{min}	0.3	0.07	-	0.34	-	-	-	0.44
$T = 1750K,\ \Delta\mu_C = -0.163eV$								
$\Delta\gamma_k(x_{min})$	0.04	0.13	-	0.27	-	-	-	0.31
x_{min}	0.32	0.11	-	0.46	-	-	-	0.47
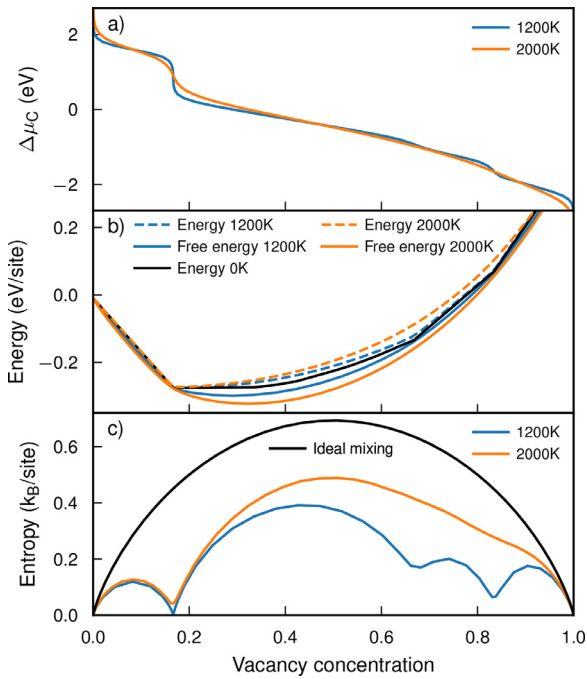
Fig. 2. Results for mixing properties from a MC simulation in the grand canonical ensemble using $k=4$. a) The chemical potential relative graphite, $\Delta\mu_C$, and the obtained averaged vacancy concentration $\langle x\rangle$. b) The mixing energy and the mixing free energy as a function of vacancy concentration. c) The mixing entropy as function of vacancy concentration, the ideal mixing entropy included for reference.

5.3. Harmonic vibrational free energy

To obtain the vibrational contribution to the the free energy (see Eq. (14)) we need to calculate the vibrational free energy for the hexagonal stacking $g_0^{har}(0, T)$ and the thin cubic film stackings $g_k^{har}(x, T)$. We use the harmonic approximation, in which, the harmonic frequencies, ω_i, are obtained from the second order force constants. The harmonic free energy can then be calculated via

$$F^{har} = \sum_i \left\{ \frac{\hbar\omega_i}{2} + k_B T \ln\left[1 - \exp(-\frac{\hbar\omega_i}{k_B T}) \right] \right\} \tag{21}$$

where the summation over i goes over all frequencies, often written as a double sum over reciprocal wave vector and band index [44,45].

Due to the very large unit cell of these structures, somewhere between 100-1500 DFT calculations are required to extract the second order force constants using PHONOPY [46] for a single configuration. This is unfeasible to do for many different stackings and vacancy concentrations. To solve this we employ force constant fitting to extract the harmonic force constants using HIPHIVE [47,48], whereas PHONOPY is used to carry out the summation in Eq. (21). This approach reduces the number of DFT calculations with an order of magnitude while still obtaining high accuracy in the free energies (see Supplemental Material for convergence analysis). This reduction allows the harmonic free energy to be computed for the lowest energy configuration at multiple vacancy concentrations and for many different stackings. The displacements of the input structures to HIPHIVE are generated from a normal distribution with a standard deviation of 0.01 Å. The details of the DFT calculations are found in Appendix A.

5.4. Anharmonic vibrational and electronic free energies

In Ref. [36] the free energy of the bulk phases of WC^{hex} and WC^{cub} was studied. It was found that anharmonicity and thermal expansion gave an important contribution to the vibrational free energy differences between WC^{hex} and WC^{cub} at high temperatures. The vibrational free energy in WC^{cub} was also found to be dependent on the carbon vacancy ordering. Further, the electronic free energy, arising from excitations of electrons, gave a significant contribution to the free energy differences.

Here, we take these effects approximately into account by using the bulk result in Ref. [36]. For $\Delta\gamma_k^{add}$, Eq. (15), the difference in additional free energy between a thin film structure and the nofilm structure enters as $g_k^{add} - g_0^{add}$. The difference between these two interface system is a few atomic layers being either cubic or hexagonal. Hence, $\Delta\gamma_k^{add}$ can be approximated by only considering the additional free energy for the cubic or hexagonal film region. This allows Eq. (15) to be approximated via

$$\Delta\gamma_k^{add}(x, T) = \frac{1}{a}\left(n_k(x)g_{cub}^{add}(x, T) - n_k(x = 0)g_{hex}^{add}(T) \right),$$

where g_{cub}^{add} and g_{hex}^{add} contains the addition in free energy per atom of the cubic and hexagonal phases, respectively. Further, $n_k(x)$ denotes the number of cubic atoms for a given stacking and vacancy concentration x. In Ref. [36] it was shown that concentration dependency of $g_{cub}^{add}(x, T)$ is weak and we, therefore, approximate it as constant over the entire concentration range.
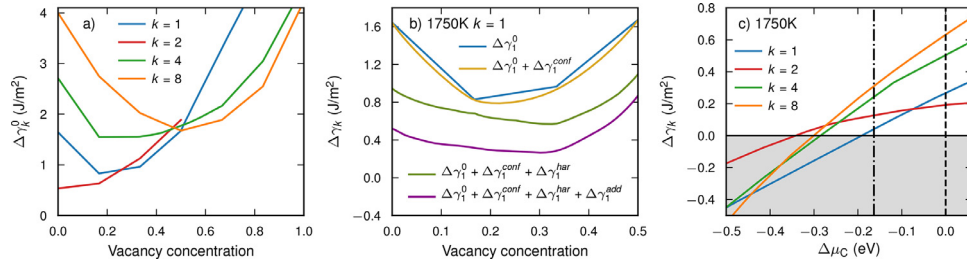
Fig. 3. a) Relative interface energy at 0K, $\Delta\gamma_k^0(x)$, as function of vacancy concentration x for $k=1$, $k=2$, $k=4$ and $k=8$. b) Relative interface energy for $k=1$ including $\Delta\gamma_k^{conf}$, $\Delta\gamma_k^{har}$ and $\Delta\gamma_k^{add}$ as function of vacancy concentration x at 1750K. c) Total relative interface energy, $\Delta\gamma_k(\Delta\mu_C, T)$, for $k=1$, $k=2$, $k=4$ and $k=8$ as function of relative carbon chemical potential $\Delta\mu_C$ at 1750 K. Dashed line indicates the graphite limit and dashed dotted line the eta (η_6) limit.

5.5. Carbon chemical potential

Finally, we need values for the carbon chemical potential $\mu_{gra}(T)$ in Eq. (9). We follow the procedure in Ref. [36] and use experimental data [49] as implemented in the Thermo-Calc software [50]. In the same way as in Ref. [36] the experimental data are aligned to the theoretical DFT data at 300 K.

Thermo-Calc is also used to extract the carbon chemical potential for the complex carbide η phases M_6C (η_6) and $M_{12}C$ (η_{12}) when in equilibrium with cobalt and WC^{hex}. These η carbon potentials are not used in any direct calculations but are used to make comparison with experimental results for W-rich materials easier. For the relevant temperatures in the present work η_6 is the stable eta phase and will be used when referring to the eta limit.

6. Results

6.1. Relative interface energy at zero Kelvin

First we consider the relative interface energies at 0 K without any carbon vacancies, $\Delta\gamma_k^0(0)$. For all stacking sequences we get positive values, as seen in Table 1. There is a clear trend that the relative interface energy increases with film thickness as expected since creating the cubic phase is associated with a large energy cost. We note that the simplified model, discussed in Sec. 2, predicts that the interface energy ought to increase with about 2.44 J/m² per cubic WC layer which fits the calculated interface energies quite well.

Next, carbon vacancies are introduced at 0K. This is done for the four selected stacking sequences, $k=1$, $k=2$, $k=4$ and $k=8$. (The selection is motivated in the Supplemental Material.) CEs are constructed and the ground-state structures for each carbon vacancy concentration are found via simulated annealing. The resulting relative interface energy, $\Delta\gamma_k^0(x)$, can be seen in Fig. 3a). By introducing carbon vacancies a substantial drop in interface energy is found, except for stacking $k=2$. In Table 1 the resulting minimum of $\Delta\gamma_k^0(x)$ is given together with the corresponding value for the carbon vacancy concentration x_{min}.

6.2. Relative interface energy at finite temperatures

The next step is to introduce the temperature dependent effects, $\Delta\gamma_k^{conf}$, $\Delta\gamma_k^{har}$ and $\Delta\gamma_k^{add}$. This is shown in Fig. 3b) for stacking sequence $k=1$ at T=1750K. Here, the relative interface energies are constructed as splines from the raw data obtained from simulations and calculations.

The configurational temperature contribution, $\Delta\gamma_k^{conf}$, is overall rather small. It vanishes at the kinks of $\Delta\gamma_k^0$ which represent strongly bounded ground state structures.

The harmonic vibrational contribution, $\Delta\gamma_k^{har}$, is larger. It shifts the minimum to larger vacancy concentration and reduces the rel-

ative interface energy with about 0.25 J/m². The vibrational contribution is somewhat anti-correlated to the energetic part $\Delta\gamma_k^0$. This reflects a general trend that atomic configurations with lower potential energy are stiffer compared to configurations of higher potential energy. Stiffer bonds corresponds to larger vibrational frequencies and, according to Eq. (21), a weaker decrease in vibrational free energy with increasing temperature.

The additional contribution $\Delta\gamma_k^{add}$ is similar in size with the harmonic vibrational contribution. $\Delta\gamma_k^{add}$ decreases with increasing vacancy concentration, which is expected as we model these additions for the WC^{cub} and WC^{hex} phases as concentration independent, see Sect. 5.4.

Finally the total relative interface energy $\Delta\gamma_k(x, T)$, defined in Eq. (11), is minimized with respect to x for given values of $\Delta\mu_C$, according to Eq. (17). The total relative interface energy $\Delta\gamma_k$ is then transformed to a function of $(\Delta\mu_C, T)$. The result is shown in Fig. 3c) for $k=1$, $k=2$, $k=4$ and $k=8$ at 1750 K. We notice that for carbon chemical potentials between the graphite and eta limits, stacking $k=1$ and $k=2$ have the lowest energies. In the graphite limit ($\Delta\mu_C = 0$ eV), the relative interface energy is equal to $\Delta\gamma_1 = 0.27$ J/m² and $\Delta\gamma_2 = 0.19$ J/m² for $k=1$ and $k=2$, respectively, and thus the films are not stable. In the eta limit ($\Delta\mu_C = -0.163$ eV) the relative interface energy is reduced due to the presence of carbon vacancies to $\Delta\gamma_1 = 0.04$ J/m² and $\Delta\gamma_2 = 0.13$ J/m². The resulting relative interface energy for $k=1$ is very small and thus the film is very close to being thermodynamically stable at 1750 K in the eta limit.

6.3. Interfacial phase diagram

We can now construct an *interfacial phase diagram*, a diagram that shows which interfacial state that is thermodynamically stable as function of temperature and carbon chemical potential. The minimization procedure, used to determine $\Delta\gamma_k$ in Fig. 3c), has to be repeated for a range of temperatures in order to find the stable stacking k as function of $\Delta\mu_C$ and T. The interfacial phase diagram for the cubic films can then be constructed and it is shown in Fig. 4. We find that the $k=1$ stacking is stable in the eta limit above 1800 K, while no thin-film stacking is stable in the graphite limit.

There are some uncertainties associated with the construction of the interfacial phase diagram. First of all the CEs constructed have an error of about 0.05J/m². Further, the term $\Delta\gamma_k^{add}$ is approximated as a bulk effect and based on our previous study concerning atomic scale modeling of the cubic and hexagonal WC bulk phases [36]. Applying these additional free energies based on the number of cubic atoms in the film is quite a crude approximation and does not consider how the additional free energy is effected by interfacial effects.

The relative interface energy, $\Delta\gamma_k$, is the difference between two similar systems and errors in the absolute interface energy
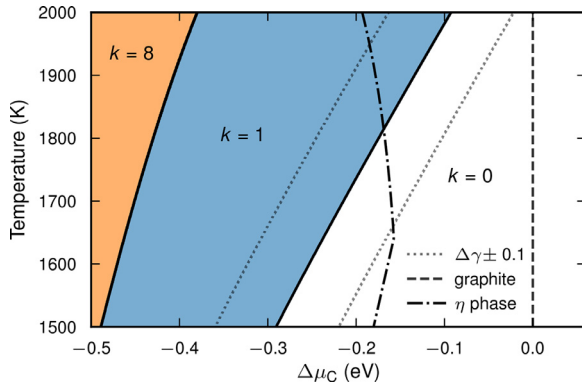
Fig. 4. Interfacial phase diagram for thin cubic films on the WC basal plane in contact with Co. The colored region indicates which stacking is thermodynamically stable, with white, blue and orange corresponding to $k=0$, $k=1$ and $k=8$ respectively. The two dotted lines show the phase-boundary between $k=0$ and $k=1$ if $\Delta\gamma$ were shifted with ± 0.1 J/m^2. The dashed line indicates the carbon potential for graphite and the dash dotted line for eta phase (η_6). The kink in the eta curve around 1600K corresponds to melting of the Co rich binder.

may to large extent cancel out. However, the error cancellation may not be complete. For example, in the present work the magnetic contribution from Co or the melting of Co have not been considered. We assume that these effects are similar in the $k=0$ system and in the other k systems and that these two effects therefore do not give significant contribution to the relative interface energy. The effect from Co melting have been shown to have a small impact on the interface free energy of a WC^{hex}(0001)/Co(111) phase boundary[51].

To explore how sensitive the phase diagram is, with respect to small changes in relative interface free energy, we calculate the shift in the stability region for $k=1$ if $\Delta\gamma_1$ were shifted with ± 0.1 J/m^2 (dotted lines in Fig. 4). This shifts the transition temperature in the eta limit by about ± 150 K.

We conclude that cubic thin films are likely thermodynamically stable (or very close to being stable) in the eta limit but not in the graphite limit at LPS temperatures. The transition to cubic thin films occurs at 1800 K (1527°C) in our present modeling study. This is in qualitative agreement with observations made in Ref. [27] where it is stated that the cubic films are frequently observed in the W-rich cemented carbide (corresponding to a low carbon potential) but seldom observed in the C-rich cemented carbide (corresponding to carbon potential close to graphite).

6.4. Layer spacing and carbon vacancy concentration

The spacing between metal layers and the carbon vacancy concentration in each layer can be determined for the films. This is done by finding the ground-state structure which best matches the obtained vacancy concentration, x_{min}, and can be seen in Table 2 for $\Delta\mu_C = -0.163$ (eta limit) and T=1750 K. The layer spacings for the films without any carbon vacancies are also given in Table 2 (inside parentheses), and shows that there is a significant reduction in spacing due to vacancies. For $k=1$ and $k=2$ this reduction mostly happens between Ml$_1$ and Ml$_2$ because the vacancies exclusively occupy the first carbon layer. Carbon vacancies in the second layer for these stackings are very energetically unfavorable due to these atomic positions being mostly hexagonal rather than cubic. For $k=4$ and $k=8$ the carbon vacancies occupy the first two carbon layers and, hence, there is a reduction of the layer spacings both between Ml$_1$ and Ml$_2$ and between Ml$_2$ and Ml$_3$.

6.5. The bulk cost

Lastly, we will look at the thickness of the cubic films obtained and why thicker films are unlikely to be stable in our modeling. The stable film found in the present work is the $k=1$ stacking, which is a very thin film with 1.5 cubic WC layers. Increasing the thickness of the film is associated with a bulk cost, $\Delta g + e$, as discussed in Sect. 2. In Table 3, values from bulk calculations of Δg, e and the strain ε are given for T=0 K and 1750 K, with and without carbon vacancies in both the graphite and eta limit.

Here, Δg values are taken from calculations done in Ref. [36]. Δg is reduced by both introducing vacancies and increasing temperature. The introduction of carbon vacancies also yields a reduction in Δg when going from the graphite limit to the eta limit.

The thin cubic films in the present work are strained (compressed) in the xy-plane to coincidence with the underlying hexagonal lattice. The values of the strain, ε, of WC^{cub} to match it with WC^{hex} is taken from bulk calculations (including thermal expansion) done in Ref. [36]. The strain energy, e, is calculated from the energy of a cubic bulk system oriented the same way the films and strained in the xy-plane. Without vacancies the cubic film is strained about 6-7%, giving rise to a large strain energy. However, when introducing 50% vacancies the lattice parameter of the cubic structure is reduced by about 4% which significantly reduces the strain of the film making the strain energy quite small.

We conclude that $\Delta g \gg e$, meaning film thickness in this case is mainly controlled via Δg.

7. Discussion

7.1. Comparison with experiments

In the present work we have explicitly computed the interfacial phase diagram for thin cubic films on the WC basal plane in contact with Co (Fig. 4) in WC-Co cemented carbides. The interfacial phase diagram shows that thin cubic films are thermodynamically stable (or very close to being stable) in the eta limit but not in the graphite limit at LPS temperatures. This is consistent with the experimental observation that cubic films are present very frequently in an W-rich material, but more seldom in an C-rich material[27].

The thermodynamically stable film, obtained in our modeling, is the one with $k=1$ stacking (Fig. 4), which has 2 cubic layers of WC. (The lower cubic WC layer in $k=1$ can also be viewed to have hexagonal stacking and hence the $k=1$ stacking can be defined to consist of 1.5 cubic layers of WC.) In our modeling thicker films are found to have higher free energies at LPS temperatures and are therefore more unlikely to form. The experimentally observed thickness of the cubic films in high resolution transmission electron microscopy (HRTEM) varies between 2-4 cubic layers of WC [23,27,28], but the exact thickness from HRTEM images is uncertain because carbon atoms are not visible. Further, observing a very thin film, e.g. $k=1$, is likely harder in HRTEM images compared with thicker films since only one W layer deviates from the hexagonal stacking. The relative interface free energy, $\Delta\gamma$, is quite small at LPS temperatures and it is therefore possible that thicker films could form due to kinetics or local fluctuations in the material. This could, for example, be a local decrease in carbon chemical potential which would create a local driving force for cubic films.

The thin cubic films might not be preserved during the cooling of the material which makes the comparison of thermodynamic stability at LPS between experimental work and our calculations more uncertain. The fact that thicker films are observed in quenched samples [28] and thinner films in normally cooled samples [27] is consistent with the fact that the free energy cost of the cubic phase is reduced at high temperatures which would allow films to grow thicker more easily. We also note that rapid cooling

Table 2

Spacing between metal (W) layers and C concentration in each C-layer in the thin films. The spacings for thin films, $k=1$, $k=2$, $k=4$ and $k=8$, are given at 1750 K and for the ground-state structures for a vacancy concentration corresponding $\Delta\mu_C = -0.163$eV. The values inside the parentheses corresponds to the layer spacing without any carbon vacancies.

k	1	2	4	8
Layer spacings (Å)				
Ml_1 - Ml_2	2.40 (2.69)	2.52 (2.73)	2.44 (2.68)	2.53 (2.69)
Ml_2 - Ml_3	2.83 (2.84)	2.84 (2.83)	2.58 (2.76)	2.41 (2.75)
Ml_3 - Ml_4	2.85 (2.85)	2.85 (2.85)	2.84 (2.83)	2.84 (2.85)
Ml_4 - Ml_5	2.85 (2.85)	2.85 (2.85)	2.85 (2.85)	2.85 (2.85)
Vacancy concentrations				
Cl_1	0.67	0.5	0.5	0.33
Cl_2	0.0	0.0	0.42	0.58
Cl_3	0.0	0.0	0.0	0.0

Table 3

Bulk (Δg) and strain (e) energies for WC^{cub} for $x=0.5$ with values for $x=0$ inside parentheses. The strain, ε is given as how much the cubic film have to be compressed in the XY-plane to match the hexagonal lattice. The strain energies at $T=1750$ K are not taking the temperature dependence of the elastic constants of WC^{cub} into account and, hence, they are upper limits of the strain energies. (The thermal expansion is larger in the cubic phase compared to the hexagonal [36], which means that the strain will increase with temperature. However, the free energy landscape $F(V)$ softens with temperature and hence the strain energy given for the strain obtained with thermal expansion is an upper limit of the correct strain free energy). The $\Delta\mu_C$ value representing equilibrium with eta phase at $T=0$ K is taken from Ref. [52].

	Δg (J/m^2)	ε (%)	e (J/m^2)
$T=0$K			
$\Delta\mu_C = 0$	0.84 (2.0)	2.0 (5.7)	0.07 (0.44)
$\Delta\mu_C = -0.292$	0.52 (2.0)	2.0 (5.7)	0.07 (0.44)
$T=1750$K			
$\Delta\mu_C = 0$	0.46 (0.77)	2.3 (7.2)	0.09 (0.69)
$\Delta\mu_C = -0.163$	0.28 (0.77)	2.3 (7.2)	0.09 (0.69)

of the cubic WC bulk phase preserves the cubic crystal structure as demonstrated in Ref. [53].

We can also compare our calculated layer spacings, given in Table 2, with experiments. Consider Fig 12(b) in Ref. [27]. The stacking of the metal layers suggests either $k=4$ or $k=8$. By inspection of Fig 12(b), we estimate the two top WC layers to have the layer spacing ~2.4 Å and the two lower ~2.9 Å. This is fully consistent with our data for stacking $k=4$ or $k=8$ and indicates a carbon vacancy concentration of about $x=0.5$ in the two topmost layers and essentially no vacancies in the two lower layers. Liu et al. [28] state a spacing of 2.384 Å for the topmost WC layers. This also indicates a substantial number of carbon vacancies in the topmost WC layers.

7.2. Grain growth inhibition

We now discuss the difference in grain growth between a C-rich and a W-rich WC-Co cemented carbide. The rate limiting process for the grain growth is the precipitation step, the addition of additional layers of WC [8,15,17].

Let us first consider the C-rich condition, where the WC grains grow without any thin cubic films present at the WC/Co phase boundaries. In Fig. 5 five steps in the growth process are shown schematically. Initially a flat interface is present (Fig. 5a). A new atomic layer is nucleated by atoms attaching to the carbide surface (Fig. 5b). This process is limited by a nucleation energy barrier. The nucleus grows laterally and eventually leading to a complete atomic layer (Fig. 5c). A second atomic layer is nucleated (Fig. 5d)

and it grows laterally. The step migration is fast compared with the nucleation process and the lateral growth can proceed until the edges of the facet has been reached before any new atomic layer is nucleated. The nucleation process is rate limiting, the grains become faceted (Fig. 5e) and the growth is purely two-dimensional.

Let us now consider the W-rich condition, where the WC grains grow with thin cubic films present at the WC/Co phase boundaries. In Fig. 6 five steps in the growth process are shown schematically. In this case a thin cubic film is present at the interface (Fig. 6a). A new atomic layer is nucleated by atoms attaching to the carbide surface (Fig. 6b). This process is assumed to be controlled by a nucleation energy barriers similar to the case without a thin cubic film present. However, in this case the lateral growth rate is substantially reduced. A thick cubic layer is energetically unfavourable and during the lateral growth the atoms in the lower lattice planes with cubic stacking have to rearrange to hexagonal stacking and carbon vacancies have to be removed through diffusion of carbon. This region is indicated by the hashed coloring in (Fig. 6c). The step migration is no longer fast compared with the nucleation process and a new atomic layer can nucleate before the lateral growth has proceeded to the edges of the facet (Fig. 6d). Hence, steps are created at the interface and the growth becomes partly three-dimensional (Fig. 6e), with a reduced overall growth rate. This is fully consistent with the well-known experimental facts that the growth rate is larger under C-rich conditions compared with W-rich conditions [8,10–14] and that steps at the interfaces are more frequent in W-rich materials compared with C-rich materials [17,22,25,26].

In general, the driving force for grain growth is the reduction of the total interface energy [15]. The phase boundary energies in C-rich and W-rich WC-Co cemented carbides are different [52]. At 0K the phase boundary energy for the basal plane ($k=0$) is 1.19 J/m^2 in the graphite limit (C-rich) and decreases gradually as function of carbon content to 0.86 J/m^2 in the eta limit (W-rich) [52]. At liquid phase sintering temperatures this difference in interface energy decreases with about 50%. Assuming this represents an average interface energy it implies that the driving force for grain growth decreases gradually from a C-rich to a W-rich material. However, in the work by Wang et al. [22] they found that after 2h of sintering, the grain size for a WC-Co material, with a composition in the middle of the carbon window, had similar grain sizes as a C-rich material. For the W-rich material they observed significantly smaller grain sizes (see their Fig. 4). Similar results were obtained by Borgh et al. [26]. They considered five different WC-Co materials, with increasing carbon contents. The two W-rich materials showed smaller grain sizes while the two C-rich and the material in the middle of the two-phase WC-Co region showed larger grain sizes (see their Fig. 3). These two experimental results demonstrate that the grain size does not change gradually between C-
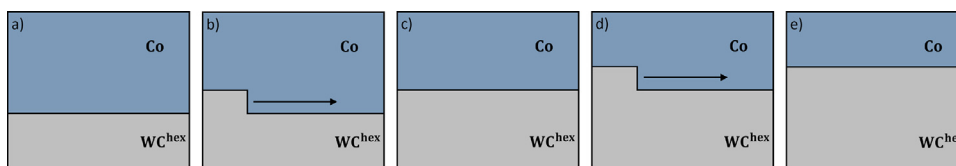
Fig. 5. a) Flat interface between hexagonal WC and Co rich binder phase. b) Lateral growth of a step in the WC interface plane. c) Flat interface from complete lateral growth. d) Lateral growth of another step in the WC interface plane. e) The growth results in perfectly faceted grains.
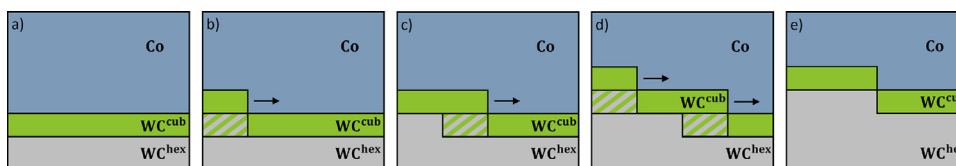
Fig. 6. a) Flat interface between hexagonal WC and Co rich binder phase with a thin film of cubic WC. b) Lateral growth of a step in the WC interface plane. The shorter arrow indicates slower growth compared to the interface without a thin film. Hatched green and grey region represents cubic WC under transformation to hexagonal WC due to equilibrium thickness of film. c) Lateral growth of the step continues. d) An additional step grows laterally before the lateral growth of the previous step has completed, leading to a partially three-dimensional growth behaviour. e) The growth results in steps at the interface.

rich and W-rich conditions, but rather changes more abruptly once approaching the W-rich limit. This can not be understood from a driving force that changes smoothly as function of carbon content, but rather supports our proposal that cubic films, which are only thermodynamically stable in W-rich materials, are related to the grain growth inhibition.

It is also interesting to compare the growth behaviour in WC-Co with doped cemented carbides. Doping cemented carbides with transition metal atoms as V, Ti, Cr, Ta, Mo and Nb is well-known to retard the grain growth [9,54]. It results in a fine grained material with increased hardness and wear resistance. The most studied and effective grain growth inhibitor is vanadium. Thin cubic films and stepped surfaces have been observed in many studies of V-doped systems [28,55–60]. Vanadium forms cubic carbide thin films at phase boundaries in cemented carbides, similarly to the formation of cubic WC in undoped cemented carbides at W-rich conditions. The vanadium-rich cubic films can form even if the bulk cubic VC phase is not thermodynamically stable [34]. This suggests that the mechanism for grain growth retardation is the same in the two different systems, however more effective in V-doped systems.

8. Conclusion

In this paper we have constructed an interfacial phase diagram for thin cubic films at the WC basal plane in contact with Co in undoped WC-Co cemented carbides. We have employed cluster expansions for modeling the carbon vacancy configurational degrees of freedom and Monte Carlo simulations to sample configurational free energies. We use a regression approach to extract the harmonic force constants which reduces the computational cost with about 90%. This reduction is enough to allow mapping out the vibrational free energy as a function of carbon vacancy concentration for multiple different stackings. Additionally, contributions from anharmonicity, thermal expansion and electronic entropy are added approximately based on our previous study of bulk WC [36].

We predict thermodynamically stable (or very close to being stable) thin cubic films at liquid phase sintering temperatures ($\sim$1450°C) in W-rich conditions, while in C-rich conditions our prediction is that the films are absent. This is in line with experimental observations [27]. It implies that the films are present at temperatures well below the temperature ($\sim$2700°C) where bulk cubic WC becomes stable. The stabilization of the thin films is due to interfacial effects and the thickness of the films is thermodynamically limited to a few atomic layers. The carbon vacancy concentra-

tion in the thin films is high and stabilizes the thin film structure while the strain effect plays a lesser role.

Based on the presence of these thin cubic films we provide a discussion on the difference in grain growth behaviour and grain structure between a W-rich and a C-rich WC-Co cemented carbide. Our argument is based on that the rate of the lateral growth of an atomic layer in a W-rich material is substantially reduced compared with a C-rich material, due to the presence of cubic stacking at phase boundaries in W-rich materials. The thickness of the cubic layers can not grow indefinitely due to thermodynamics and therefore, in the growth process, the cubic stacking has to be transformed to hexagonal stacking. This delays the growth and the grains becomes smaller in W-rich materials. Further, the presence of the thin cubic films at the phase boundaries in W-rich materials shifts the balance between initial nucleation process and the following lateral growth and makes steps more likely at the phase boundaries. The growth becomes partly three-dimensional.

Both the slower growth rate and the occurrence of steps at the phase boundaries in W-rich materials are well established experimentally [8,10–14,17,22,25,26] and here we provide an explanation based on the tendency to form cubic structures at phase boundaries in W-rich cemented carbides.

Declaration of Competing Interest

The authors declare that they have no known competing financial interests or personal relationships that could have appeared to influence the work reported in this paper.

Acknowledgments

Appendix A. Electronic structure calculations

DFT as implemented in the Vienna ab initio simulation package (VASP) [61,62] is utilized for the electronic structure calculations in this study. The included projector-augmented wave (PAW) [63,64] potentials and the Perdew, Burke, and Ernzerhof (PBE) exchange–correlation functional [65] are used in all calculations. Further, the smearing method of Methfessel and Paxton to first order with a smearing width of 0.1 [66] is used and the Brillouin zone is sampled using a Γ-centered grid.

The thin film systems, as described in Sect. 3, are constructed by stacking a slab of fcc Co with 7 atomic layers in the [111] directions on top of a slab of hexagonal WC with two W-terminated (0001) surfaces and a total of 6 (5) atomic layers of W (C) in the [0001] direction. In order to end up with one phase boundary under periodic boundary conditions 10 Å of vacuum is added perpendicular to the interface plane between the two remaining Co (111) and WC (0001) planes, thus creating two free surfaces. The stacking of W and C layers at the interface is subsequently altered to get various thin film systems according to Fig. 1. In the parallel direction the size of the system is determined by the hexagonal WC phase. The unit cell in the interface plane is a parallelogram with base $\sqrt{3}a_{\mathrm{WC}}$ and height $(3/2)a_{\mathrm{WC}}$, where a_{WC} is the bulk lattice constant for WC$^{\mathrm{hex}}$ (see Ref. [34] for a figure of the unit cell). Our DFT values for the bulk lattice constants are $a_{\mathrm{WC}} = 2.915$ Å and $c_{\mathrm{WC}} = 2.844$ Å. In all our VASP calculations of the thin film system a 2x2 supercell in the interface plane is used, which implies that our slab system contains 244 atoms for a system without C vacancies. Further, 5 k-points along each reciprocal lattice vector in the interface plane and 1 k-point along the reciprocal lattice vector perpendicular to the interface plane are used. This corresponds to a k-point density of 8.04 Å in the interface plane. Reference bulk calculations are done with better or equal k-point density.

When calculating the reference energy used for training the cluster-expansions a plane-wave cutoff of 400 eV is used and the ionic positions are optimized until all forces were below 0.02 eV/Å.

For constructing the vibrational models, more accurate forces are required, and to this end we use a higher plane-wave cutoff of 520 eV and evaluate the projection operators in reciprocal space, i.e LREAL=.FALSE.. Additionally, the ionic positions are optimized until all forces are below 0.005 eV/Å. The plane-wave cut-off is chosen such that the vibrational free energy is converged.

In order to limit the computational cost we model the systems using non-spinpolarized calculations even though the Co phase has a ferromagnetic ground state. However, this study only considers relative interface energies and the difference in energy between various stackings and the vacancy formation energies in WC are quite insensitive to the magnetic state of the binder phase.

Supplementary material

Supplementary material associated with this article can be found, in the online version, at doi:10.1016/j.actamat.2021.117128

References

[1] R.M. German, P. Suri, S.J. Park, Review: liquid phase sintering, J. Mater. Sci. 44 (1) (2009) 1–39, doi:10.1007/s10853-008-3008-0.

[2] H.E. Exner, Physical and chemical nature of cemented carbides, Int. Mater. Rev. 24 (1) (1979) 149–173, doi:10.1179/imtr.1979.24.1.149.

[3] Z.Z. Fang, X. Wang, T. Ryu, K.S. Hwang, H.Y. Sohn, Synthesis and mechanical properties of nanocrystalline cemented tungsten carbide – A review, Int. J. Refract. Met. Hard Mater. 27 (2) (2009) 288–299, doi:10.1016/j.ijrmhm.2008.07.011.

[4] G. Upadhyaya, Materials science of cemented carbides - an overview, Mater. Des. 22 (6) (2001) 483–489, doi:10.1016/S0261-3069(01)00007-3.

[5] H.O. Andrén, Microstructures of cemented carbides, Mater. Des. 22 (2001) 491, doi:10.1016/S0261-3069(01)00006-1.

[6] L. Prakash, 1.02 - Fundamentals and general applications of hardmetals, in: V.K. Sarin (Ed.), Comprehensive Hard Materials, Elsevier, Oxford, 2014, p. 29, doi:10.1016/B978-0-08-096527-7.00002-7.

[7] S. Norgren, J. García, A. Blomqvist, L. Yin, Trends in the P/M hard metal industry, Int. J. Refract. Met. Hard Mater. 48 (2015) 31–45, doi:10.1016/j.ijrmhm.2014.07.007.

[8] C.H. Allibert, Sintering features of cemented carbides WC-Co processed from fine powders, Int. J. Refract. Met. Hard Mater. 19 (2001) 53, doi:10.1016/S0263-4368(01)00004-X.

[9] J. Garca, V.C. Ciprs, A. Blomqvist, B. Kaplan, Cemented carbide microstructures: a review, Int. J. Refract. Met. Hard Mater. 80 (2019) 40–68, doi:10.1016/j.ijrmhm.2018.12.004.

[10] J. Gurland, A study of the effect of carbon content on the structure and properties of sintered WC-Co alloys, J. Met. (1954) 285–290.

[11] H. Suzuki, M. Sugiyama, T. Umeda, Effect of the carbon content on properties of WC-10%Co alloy, J. Jpn I. Met. 28 (1964) 55–58, doi:10.2320/jinstmet1952.28.2_55.

[12] G.J. Rees, B. Young, A study of the factors controlling grain size in sintered hard-metal, Powder Metall. 14 (27) (1971) 185–198, doi:10.1179/pom.1971.14.27.014.

[13] V. Chabretou, C.H. Allibert, J.M. Missiaen, Quantitative analysis of the effect of the binder phase composition on grain growth in WC-Co sintered materials, J. Mater. Sci. 38 (2003) 2581, doi:10.1023/A:1024418131674.

[14] S. Lay, J.M. Missiaen, 1.03 - microstructure and morphology of hardmetals, in: V.K. Sarin (Ed.), Comprehensive Hard Materials, Elsevier, Oxford, 2014, p. 91, doi:10.1016/B978-0-08-096527-7.00003-9.

[15] K. Mannesson, J. Jeppsson, A. Borgenstam, J. Ågren, Carbide grain growth in cemented carbides, Acta Mater. 59 (2011) 1912, doi:10.1016/j.actamat.2010.11.056. http://www.sciencedirect.com/science/article/pii/S1359645410008116

[16] O. Lavergne, C.H. Allibert, Dissolution mechanism of tungsten carbide in cobalt-based liquids, high temperatures, High Press. (Print) 31 (3) (1999) 347–355.

[17] Z. Roulon, J. Missiaen, S. Lay, Carbide grain growth in cemented carbides sintered with alternative binders, Int. J. Refract. Met. Hard Mater. 86 (2020) 105088, doi:10.1016/j.ijrmhm.2019.105088. http://www.sciencedirect.com/science/article/pii/S0263436819304664

[18] Y. Kim, N. Hwang, D. Yoon, Abnormal growth of faceted (WC) grains in a (Co) liquid matrix, Metall. Mater. Trans. A 27 (1996) 2809, doi:10.1007/BF02652373.

[19] G.S. Rohrer, C.L. Rohrer, W.W. Mullins, Coarsening of faceted crystals, J. Am. Ceram. Soc. 85 (3) (2002) 675–682, doi:10.1111/j.1151-2916.2002.tb00149.x.

[20] W.K. Burton, N. Cabrera, F.C. Frank, N.F. Mott, The growth of crystals and the equilibrium structure of their surfaces, Philos. Trans. R. Soc. London Ser. A 243 (866) (1951) 299–358, doi:10.1098/rsta.1951.0006.

[21] Y. Zhong, L.L. Shaw, Growth mechanisms of WC in WC-5.75wt% Co, Ceram. Int. 37 (8) (2011) 3591–3597, doi:10.1016/j.ceramint.2011.06.016.

[22] Y. Wang, M. Heusch, S. Lay, C. Allibert, Microstructure evolution in the cemented carbides WC-Co I. Effect of the C/W ratio on the morphology and defects of the WC grains, Phys. Status Solidi A 193 (2002) 271, doi:10.1002/1521-396X(200209)193:2<271::AID-PSSA271>3.0.CO;2-O.

[23] S. Lay, C.H. Allibert, M. Christensen, G. Wahnström, Morphology of WC grains in WC–Co alloys, Mat. Sci. Eng. A-Struct. 486 (1) (2008) 253–261, doi:10.1016/j.msea.2007.09.019.

[24] A. Delanoë, S. Lay, Evolution of the WC grain shape in WC-Co alloys during sintering: Effect of C content, Int. J. Refract. Met. Hard Mater. 27 (1) (2009) 140–148, doi:10.1016/j.ijrmhm.2008.06.001. http://www.sciencedirect.com/science/article/pii/S026343680800067X

[25] S. Kim, S.-H. Han, J.-K. Park, H.E. Kim, Variation of wc grain shape with carbon content in the wc-co alloys during liquid-phase sintering, Scripta Mater. 48 (5) (2003) 635–639, doi:10.1016/S1359-6462(02)00464-5.

[26] I. Borgh, P. Hedström, T. Persson, S. Norgren, A. Borgenstam, J. Ågren, J. Odqvist, Microstructure, grain size distribution and grain shape in WC–co alloys sintered at different carbon activities, Int. J. Refract. Met. Hard Mater 43 (2014) 205–211, doi:10.1016/j.ijrmhm.2013.12.007.

[27] V. Bounhoure, S. Lay, M. Loubradou, J.M. Missiaen, Special WC/Co orientation relationships at basal facets of WC grains in WC–Co alloys, J. Mater. Sci. 43 (3) (2008) 892–899, doi:10.1007/s10853-007-2181-x.

[28] X. Liu, X. Song, H. Wang, X. Liu, F. Tang, H. Lu, Complexions in WC-Co cemented carbides, Acta Mater. 149 (2018) 164–178, doi:10.1016/j.actamat.2018.02.018.

[29] A.S. Kurlov, A.I. Gusev, Tungsten carbides and W-C phase diagram, Inorg. Mater. 42 (2) (2006) 121–127, doi:10.1134/S0020168506020051.

[30] S.A.E. Johansson, G. Wahnström, First-principles derived complexion diagrams for phase boundaries in doped cemented carbides, Curr. Opin. Solid St. M. 20 (5) (2016) 299–307, doi:10.1016/j.cossms.2016.05.009.

[31] P.R. Cantwell, M. Tang, S.J. Dillon, J. Luo, G.S. Rohrer, M.P. Harmer, Grain boundary complexions, Acta Mater. 62 (2014) 1–48, doi:10.1016/j.actamat.2013.07.037.

[32] P.R. Cantwell, T. Frolov, T.J. Rupert, A.R. Krause, C.J. Marvel, G.S. Rohrer, J.M. Rickman, M.P. Harmer, Grain boundary complexion transitions, Annu. Rev. Mater. Res. 50 (1) (2020) 465–492, doi:10.1146/annurev-matsci-081619-114055.

[33] S.A.E. Johansson, G. Wahnström, Theory of ultrathin films at metal–ceramic interfaces, Philos. Mag. Lett. 90 (8) (2010) 599–609, doi:10.1080/09500831003800863.

[34] S.A.E. Johansson, G. Wahnström, First-principles study of an interfacial phase diagram in the V-doped WC-Co system, Phys. Rev. B 86 (3) (2012) 035403, doi:10.1103/PhysRevB.86.035403.

[35] A. Stukowski, Visualization and analysis of atomistic simulation data with OVITO–the open visualization tool, Model. Simul. Mater. Sci.Eng. 18 (1) (2009) 015012, doi:10.1088/0965-0393/18/1/015012.

[36] M. Gren, E. Fransson, M. Ångqvist, P. Erhart, G. Wahnström, Modeling of vibrational and configurational degrees of freedom in hexagonal and cubic tungsten carbide at high temperatures, Phys. Rev. Materials 5 (2021) 033804, doi:10.1103/PhysRevMaterials.5.033804.

[37] A. Sutton, R. Balluffi, Interfaces in Crystalline Materials, Clarendon Press, 1997.

[38] J. Sanchez, F. Ducastelle, D. Gratias, Generalized cluster description of multicomponent systems, Physica A 128 (1) (1984) 334–350, doi:10.1016/0378-4371(84)90096-7.

[39] D. de Fontaine, Cluster approach to order-disorder transformations in alloys, in: H. Ehrenreich, D. Turnbull (Eds.), Solid State Physics, volume 47, Academic Press, 1994, p. 33, doi:10.1016/S0081-1947(08)60639-6.

[40] M. Ångqvist, W.A. Muñoz, J.M. Rahm, E. Fransson, C. Durniak, P. Rozyczko, T.H. Rod, P. Erhart, ICET – a python library for constructing and sampling alloy cluster expansions, Adv. Theory Simul. 0 (0) (2019) 1900015, doi:10.1002/adts.201900015.

[41] N. Metropolis, A.W. Rosenbluth, M.N. Rosenbluth, A.H. Teller, E. Teller, Equation of state calculations by fast computing machines, J Chem. Phys. 21 (1953) 1087, doi:10.1063/1.1699114.

[42] D. Frenkel, B. Smit, Understanding Molecular Simulation: From Algorithms to Applications, Computational Science Series, 1, Academic Press, 2001.

[43] B. Sadigh, P. Erhart, Calculation of excess free energies of precipitates via direct thermodynamic integration across phase boundaries, Phys. Rev. B 86 (13) (2012) 134204, doi:10.1103/PhysRevB.86.134204.

[44] D.C. Wallace, Thermodynamics of Crystals, Wiley, 1972.

[45] B. Fultz, Vibrational thermodynamics of materials, Prog. Mater Sci. 55 (4) (2010) 247–352, doi:10.1016/j.pmatsci.2009.05.002.

[46] A. Togo, I. Tanaka, First principles phonon calculations in materials science, Scr. Mater. 108 (2015) 1–5, doi:10.1016/j.scriptamat.2015.07.021. http://www.sciencedirect.com/science/article/pii/S1359646215003127

[47] F. Eriksson, E. Fransson, P. Erhart, The Hiphive Package for the Extraction of High-Order Force Constants by Machine Learning, Adv. Theory Simul. 0 (0) (2019) 1800184, doi:10.1002/adts.201800184.

[48] E. Fransson, F. Eriksson, P. Erhart, Efficient construction of linear models in materials modeling and applications to force constant expansions, NPJ Comput. Mater.. 6(1) 10.1038/s41524-020-00404-5.

[49] P. Gustafson, An evaluation of the thermodynamic properties and the P, T phase diagram of carbon, Carbon 24 (1986) 169, doi:10.1016/0008-6223(86)90113-2.

[50] J.-O. Andersson, T. Helander, L. Höglund, P. Shi, B. Sundman, Thermo-Calc & DICTRA, computational tools for materials science, Calphad 26 (2) (2002) 273–312, doi:10.1016/S0364-5916(02)00037-8.

[51] M.A. Gren, E. Fransson, G. Wahnström, A computational study of the temperature dependence of interface and surface energies in WC-Co cemented carbides, Int. J. Refract. Met. Hard Mater. 87 (2020) 105114, doi:10.1016/j.ijrmhm.2019.105114. http://www.sciencedirect.com/science/article/pii/S026343681930455X

[52] M.V.G. Petisme, S.A.E. Johansson, G. Wahnström, A computational study of interfaces in WC–Co cemented carbides, Model. Simul. Mater. Sc. 23 (2015) 045001, doi:10.1088/0965-0393/23/4/045001.

[53] R.H. Willens, E. Buehler, B.T. Matthias, Superconductivity of the transition-metal carbides, Phys. Rev. 159 (1967) 327–330, doi:10.1103/PhysRev.159.327.

[54] S. Farag, I. Konyashin, B. Ries, The influence of grain growth inhibitors on the microstructure and properties of submicron, ultrafine and nano-structured hardmetals – a review, Int. J. Refract. Metals and Hard Mater. 77 (2018) 12–30, doi:10.1016/j.ijrmhm.2018.07.003.

[55] T. Yamamoto, Y. Ikuhara, T. Sakuma, High resolution transmission electron microscopy study in VC-doped WC-Co compound, Sci. Technol. Adv. Mater. 1 (2) (2000) 97–104, doi:10.1016/S1468-6996(00)00006-1.

[56] S. Lay, J. Thibault, S. Hamar-Thibault, Structure and role of the interfacial layers in VC-rich WC-Co cermets, Philos. Mag. 83 (10) (2003) 1175–1190, doi:10.1080/1478643031000075759.

[57] S. Lay, M. Loubradou, P. Donnadieu, Ultra fine microstructure in WC-Co cermet, Adv. Eng. Mater. 6 (10) (2004) 811–814, doi:10.1002/adem.200400084.

[58] I. Sugiyama, Y. Mizumukai, T. Taniuchi, K. Okada, F. Shirase, T. Tanase, Y. Ikuhara, T. Yamamoto, Formation of (W,V)Cx layers at the WC/Co interfaces in the VC-doped WC-Co cemented carbide, Inte. J. Refract. Metals Hard Mater. 30 (1) (2012) 185–187, doi:10.1016/j.ijrmhm.2011.08.006. http://www.sciencedirect.com/science/article/pii/S026343681100151X

[59] I. Sugiyama, Y. Mizumukai, T. Taniuchi, K. Okada, F. Shirase, T. Tanase, Y. Ikuhara, T. Yamamoto, Three-dimensional morphology of (W,V)Cx in VC-doped WC-Co hard metals, Scripta Materialia 69 (6) (2013) 473–476, doi:10.1016/j.scriptamat.2013.06.002. http://www.sciencedirect.com/science/article/pii/S1359646213003047

[60] K. Okada, A. Osada, Microstructural study on the grain growth inhibition of vc-doped WC-Co cemented carbides, Int. J. Refract. Metals Hard Mater. 62 (2017) 149–154, doi:10.1016/j.ijrmhm.2016.06.009. Hardmetals - raw materials, technologies and applications

[61] G. Kresse, J. Furthmüller, Efficient iterative schemes for ab initio total-energy calculations using a plane-wave basis set, Phys. Rev. B 54 (1996) 11169, doi:10.1103/PhysRevB.54.11169.

[62] G. Kresse, J. Furthmüller, Efficiency of ab-initio total energy calculations for metals and semiconductors using a plane-wave basis set, Comp. Mater. Sci. 6 (1996) 15, doi:10.1016/0927-0256(96)00008-0.

[63] P.E. Blöchl, Projector augmented-wave method, Phys. Rev. B 50 (1994) 17953–17979, doi:10.1103/PhysRevB.50.17953.

[64] G. Kresse, D. Joubert, From ultrasoft pseudopotentials to the projector augmented-wave method, Phys. Rev. B 59 (1999) 1758, doi:10.1103/PhysRevB.59.1758.

[65] J.P. Perdew, K. Burke, M. Ernzerhof, Generalized gradient approximation made simple, Phys. Rev. Lett. 77 (1996) 3865, doi:10.1103/PhysRevLett.77.3865.

[66] M. Methfessel, A.T. Paxton, High-precision sampling for Brillouin-zone integration in metals, Phys. Rev. B 40 (1989) 3616, doi:10.1103/PhysRevB.40.3616.